Nanoscale deformation mechanisms and yield properties of hydrated bone extracellular matrix

Nanoscale deformation mechanisms and yield properties of hydrated bone extracellular matrix

Jakob Schwiedrzik[a,*], Aidan Taylor[a,1], Daniele Casari[a], Uwe Wolfram[c], Philippe Zysset[b], Johann Michler[a]

[a] *Empa Swiss Federal Laboratory for Material Science and Technology, Laboratory of Mechanics of Materials and Nanostructures, Thun, Switzerland*
[b] *Institute for Surgical Technology and Biomechanics, University of Bern, Switzerland*
[c] *Institute for Mechanical, Process and Energy Engineering, Heriot Watt University, Edinburgh, UK*

Abstract

Bone features a hierarchical architecture combining antagonistic properties like toughness and strength. In order to better understand the mechanisms leading to this advantageous combination, its postyield and failure behavior was analyzed on the length scale of a single lamella. Micropillars were compressed to large strains under hydrated conditions to measure their anisotropic yield and post-yield behavior. An increase in strength compared to the macroscale by a factor of 1.55 and a strong influence of hydration with a decrease by 60% in yield stress compared to vacuum conditions were observed. Post-compression transmission electron microscopic analysis revealed anisotropic deformation mechanisms. In axial pillars, where fibrils were oriented along the loading axis, kink bands were observed and shear cracks emerged at the interface of ordered and disordered regions. Micromechanical analysis of fibril kinking allowed an estimate of the extrafibrillar matrix shear strength to be made: 120 ± 40 MPa . When two opposing shear planes met a wedge was formed, splitting the micropillar axially in a mode 1 crack. Making use of an analytical solution, the mode 1 fracture toughness of bone extracellular matrix for splitting along the fibril direction was estimated to be 0.07 MPa$\sqrt{m}$. This is 1-2 orders of magnitude smaller than on the macroscale, which may be explained by the absence of extrinsic toughening mechanisms. In transverse pillars, where fibrils were oriented perpendicular to the loading axis, cracks formed in regions where adverse fibril orientation reduced the local fracture resistance. This study underlines the importance of bone's hierarchical microstructure for its macroscopic strength and fracture resistance and the need to

*Corresponding author. Email: jakob.schwiedrzik@empa.ch
[1] Current address: Microscopy and Microanalysis Facility, University of California, Santa Barbara, USA

study structure-property relationships as well as failure mechanisms under hydrated conditions on all length scales.

Keywords: Bone extracellular matrix, micromechanics, yielding, deformation mechanisms

1. Introduction

Bone is a biological material featuring a hierarchical architecture combining antagonistic properties like toughness and strength with a low specific weight. In order to better understand the mechanisms leading to this advantageous combination of attributes, its mechanical behaviour has to be assessed on all length scales.

Bone provides mechanical support to the musculoskeletal system, metabolizes calcium and produces bone marrow [1, 2]. On the nanoscale, it is made up of parallel mineralized collagen fibrils (MCF) embedded in an extrafibrillar mineral matrix (EFM) consisting of mineral, non-collageneous proteins and water [3, 1, 2]. The MCF line up in fibril arrays, which form lamellae in a rotated plywood pattern [4]. Osteocytes and their processes reside in the lacuno-canalicular system, which makes up for about 1% of bone porosity. Compact or cortical bone consists of lamellae arranged concentrically around blood vessels forming osteons surrounded by a cement layer with a porosity of around 5-15% [2]. In large, fast growing animals fibrolamellar or plexiform bone is laid out first before it is converted to osteonal bone through a remodeling process [5, 2].

Macroscopic mechanical tests on bone have been performed for more than a century [5, 6]. However, several challenges remain, mostly due to spatial, inter-subject, disease or age variation. Considering bone as a hierarchical material and probing its properties on several length scales is of high relevance as its inelastic behaviour at a lower level of tissue organisation influences the mechanical behaviour of the whole organ.

On the macroscale, bone is known to react to overloading mainly by formation and coalescence of families of microcracks, whose orientation depend on the loading mode [7, 8, 6], leading to a quasi-brittle response. On the nanoscale, *in situ* small angle x-ray scattering (SAXS) and wide angle x-ray diffraction (WAXD) measurements under tensile loading showed that mineral platelets carry a significant portion of the load and are insensitive to internal flaws due to size effects [9]. The organic phase transfers the load to the mineral platelets; it was shown that apparent yielding in parallel-fibred bone was caused by inelastic deformation of the extrafibrillar matrix [10]. Interpre-

tation of measured yield stresses at variable temperature and strain rate using an *Arrhenius*-type rate equation revealed the activation energy and volume of the underlying deformation mechanism to be around 1 eV and 1 nm^3, respectively, corresponding to charge interactions between molecules in the extrafibrillar matrix [11]. Furthermore, it was suggested that ion-mediated organic networks featuring sacrificial bonds and hidden length are a major determinant for bone toughness [12]. It was shown that toughness increased significantly in the presence of Ca^{2+} ions, which also hints at the presence of an ion-mediated organic glue between mineralised collagen fibrils [13].

These experiments shed light on the possible deformation mechanisms of bone on the nanoscale. However, when testing specimens of hundreds of micrometers to millimetres in size, the measured data is integrated over the response of several structural units including inhomogeneities like cement interfaces, pores, changes in fibril orientation and mineral content, as well as extrinsic toughening mechanisms caused by the multiscale microarchitecture [14, 15, 16, 17]. As a consequence, interpretation in terms of the local deformation mechanisms or yield properties on the length scale of a single lamella is not easily extracted. Therefore, micromechanical testing methods are an attractive alternative for answering this question.

One of the most common micromechanical testing techniques for bone is microindentation [18, 19, 20, 21]. A diamond probe with a known geometry, e.g. a three sided pyramid, is pressed into a polished sample surface and force and tip displacement are recorded simultaneously. Elastic properties may be extracted from the elastic unloading part of the indentation curve using contact mechanics [22]. The mean indentation pressure, or hardness, is related to the yield and post-yield characteristics of the studied material [23]. However, it is very difficult to uniquely interpret indentation curves in terms of nonlinear material behaviour unless the dissipative mechanisms are very well understood [24, 25]. Therefore, there is a need for independent experiments assessing the yield and failure properties as well as deformation mechanisms of bone on the extracellular matrix (ECM) level.

Such an alternative experimental setup is micropillar compression [26, 27, 28]. Micron sized pillars are produced by erosion of material using a focussed ion beam (FIB) and compressed with a flat punch diamond indenter. Due to the mostly uniaxial loading conditions [29], the interpretation of the resulting force-displacement curves in terms of stress-strain behaviour is relatively straightforward. This is a clear advantage when assessing yield properties compared to microindentation, which results in a heterogeneous and multiaxial stress state under the indenter [23].

Recently, this method has been applied to lamellar bone tissue [28, 30, 31] in the dry condition. An increased strength and ductility was found in all studies compared to macroscopic properties. Also, an absence of damage was noted at strain levels up to 8 % [28]. However, several studies have shown that the hydration state of the sample is an important factor influencing the properties on several length scales [32, 33, 20, 34, 35]. Therefore, it is desirable to perform micropillar compression experiments on bone extracellular matrix under rehydrated conditions in order to obtain its physiologically relevant yield and failure properties. Finally, as failure is a highly localized phenomenon, probing small pieces of bone with a minimum of interfaces or flaws under controlled boundary conditions allows large inelastic strains in the sample to accumulate at known stress levels. This in turn can be used to reveal further insights into the nanoscale deformation mechanisms when combined with post-test analytical methods like transmission electron microscopy (TEM).

The aims of this study were to a) develop a setup and protocol for micropillar compression under hydrated conditions, b) measure the anisotropic compressive yield and failure properties, c) visualize the anisotropic deformation mechanisms under uniaxial loading, and d) interpret the findings by combining models of the observed failure mechanisms with a continuum micromechanical description of the extracellular matrix. Microindentations were performed in the axial and transverse directions in ovine osteonal bone hydrated in Hank's buffered saline solution (HBSS) [28]. Micropillars were also prepared in the axial and transverse directions, rehydrated in HBSS and compressed under liquid immersion. The results were compared to micropillar compression in vacuum [28], dry and hydrated nanoindentation [28], as well as macroscopic data from the literature [36]. Approximately 200 nm thin lamellae were prepared from tested micropillars in then axial and transverse directions as well as unloaded controls and analysed using Scanning Transmission Electron Microscopy (STEM) and Selected Area Diffraction (SAD) to determine the governing deformation mechanism of hydrated bone extracellular matrix under uniaxial compression as a function of microstructure. Finally, micromechanical modelling was combined with analytical solutions for the observed failure mechanisms in order estimate the mode 1 fracture toughness of ECM for splitting along the fibre direction as well as the shear strength of the EFM.

2. Materials & Methods

2.1. Sample preparation

Two ovine tibiae were acquired from a local abattoir. Axial and transverse specimens were cut from the diaphyses with a diamond-coated band saw (Exact, Germany) and embedded in but not infiltrated by Cu-filled polymethyl methacrylate (PMMA, Technovit 5000, Heraeus, Germany). The embedded specimens were glued onto scanning electron microscope (SEM) stubs with conductive Ag-filled adhesive, air-dried and ultramilled with diamond blades (Polycut E, Reichert-Jung, Germany) in order to obtain a flat and smooth surface for the microindentation and micropillar compression experiments.

A 20 nm thick Au-Pd film was sputtered on the specimens to minimise drift due to charging under the electron or ion beams. A dual beam FIB workstation (Tescan Lyra, Czech Republic) with a Ga^+ column operated at 30 kV was used to machine micropillars of 5 µm diameter and aspect ratio of 2 in osteonal regions using an established protocol [28]. Monte Carlo simulations assessing FIB damage on the side of the pillar using the SRIM code [37] have shown that FIB damage and Ga^+ ion implantation may be neglected due to the thin influenced layer (25 nm) and the comparatively large size of the pillars (5 µm) [28]. This was verified in this study by means of STEM analysis of FIB-milled pillars, which showed an influence zone of no more than 30 nm thickness on the side or the top of the pillars as will be discussed in detail later.

2.2. Mechanical testing and analysis

Microindentations in wet and dry conditions were performed in a previous study [28] in osteonal regions of the same bone using a UNHT system with a long shaft Berkovich indenter and active surface referencing (Anton Paar TriTec, Switzerland). Samples were rehydrated for 2 h in HBSS prior to loading. Indentations were performed in load control up to a maximum depth of 1 µm with a loading rate of 100 mN/min, holding time of 30 s and unloading rate of 400 mN/min in order to minimize the effects of creep [33]. Plain strain modulus and indentation hardness, which is defined as the maximum load divided by the contact area at maximum depth were extracted using the method of Oliver and Pharr [22].

A total of 24 micropillars of 5 µm diameter and aspect ratio of 2 were fabricated in the axial (13) and transverse specimens (11) and used for quasi-static, monotonic compression experiments.

Samples were rehydrated for 2 h in HBSS. Directly before the start of the loading protocol, the HBSS level inside the cell was reduced so that the sample surface was directly accessible. It was verified using an optical microscope that the micropillars stayed completely submerged in HBSS in the surrounding FIB trench. Compression of the micropillars was carried out under hydrated conditions using a UNHT system (Anton Paar TriTec, Switzerland) equipped with a long shaft flat punch indenter (20 µm diameter) and reference as well as a custom made liquid cell. The micropillars were compressed in load control at a loading rate of 5 mNs^{-1}, which led to strain rates in the micropillars of $1 \cdot 10^{-4} s^{-1}$ to $5 \cdot 10^{-4} s^{-1}$ in the linear elastic region up to yielding. Samples were unloaded at 5 mNs^{-1} once they showed significant yielding along with a considerable increase in apparent strain rate. After testing, it was again verified that the trenches of the micropillars were still filled with HBSS, thereby guaranteeing tests under fully hydrated conditions. Fig. 1 shows a sketch of the experimental setup with the micropillars submerged in HBSS inside the FIB trench.

All micropillars were imaged after compression using a high resolution FIB/SEM work station (Tescan Lyra, Czech Republic) operated at 5 kV and 55° specimen tilt. Based on the pre- and post-test images, 2 axial and 2 transverse samples were removed from the study, as the images showed either an irregular pre-test shape or excessive bending of the pillars – most probably due to inhomogeneities in the substrate. The remaining 20 load-displacement datasets were corrected for pillar sink-in using the modified Sneddon approach [38] with a fillet radius of 300 nm following an established protocol [28]. This approach allows to correct apparent strains for elastic sink-in of the pillar into the bone substrate using the analytical model of Sneddon of a flat punch indentation on an elastic halfspace [39] modified to allow a fillet radius at the bottom of the pillar [38].

Engineering stress-strain data was obtained by dividing the force by the top cross sectional area and tip displacement by the height of each micropillar and converted to true stress-strain data using the assumption of negligible volume change [40]. Apparent loading modulus was defined as the maximum slope of the loading curve found using a moving regression with constant window size. True yield stress was determined using a 0.4% strain offset rule, ultimate stress is defined as the maximum stress in the true stress-strain curve. The high value strain offset of 0.4% was chosen to be consistent with the experimental uncertainties in strain measurement in micropillar compression due to the presence of a toe region and inelastic sink-in as well as the high strains reached throughout the experiments.

2.3. Statistics

Statistical analysis was performed using R [41]. Parametric statistical tests were used due to the limited sample number. Measurements are reported as mean ± standard deviation.

2.4. Imaging

Two axial and one transverse pillar with representative yield stresses and failure patterns were chosen for further analysis by TEM. The micropillars and neighbouring regions of undeformed material within the same osteon were coated with a Pt layer by focussed electron beam induced deposition (FEBID) and focussed ion beam induced deposition (FIBID) in a FIB/SEM workstation (Tescan Lyra, Czech Republic) in order to protect them from excessive ion beam damage. Trenches were milled at 30 kV and 1600 pA and the resulting lamellae were polished down to a thickness of 2 µm using an acceleration voltage of 30 kV and beam current of 350 pA. A tungsten needle on a nanomanipulator (Alemnis, Switzerland) was attached to the lamella using Pt FIBID. Subsequently, the lamellae were cut free using the ion beam at 30 kV and 50 pA and the lamellae lifted out and transferred onto a Cu TEM grid using Pt FIBID. In a second step, the lamellae were further polished to a thickness of approximately 200 nm in 3 steps (15 kV, 400 pA; 10 kV, 100 pA; 5 kV, 50 pA). Stepping down the voltage in this manner helps to reduce the gallium implantation and surface damage associated with FIB TEM lamella preparation. Bright field (BF-STEM) and selected area diffraction (SAD) patterns with a virtual detector distance of 40 cm and a spot size of 1.5 µm were taken at 200 kV in a TEM (JEM2200FS, JEOL, Japan). A small condenser aperture and a spread bead were used to limit beam damage to the samples. Additional BF-STEM of undeformed regions from the same bone was performed using a transmitted electron detector in an HRSEM (Hitachi S-4800, Japan) operated at 30 kV accelerating voltage. For this, several TEM lamellae were prepared in the axial-radial plane of an osteon. 2D Fast Fourier Transformations (FFTs) of areas with visible collagen banding were performed using ImageJ to reveal the collagen fibril orientation.

2.5. Mechanical modeling

2.5.1. Continuum micromechanics

The elastic properties of bone ECM and EFM were estimated using continuum micromechanics, which relates the effective stiffness tensor of a representative volume element (RVE) to its

microstructure and the elastic properties and volume fractions of its constituents by [42]

$$\mathbb{S}_{eff} = \Big(\sum_{i=1,n} \phi_i \mathbb{S}_i \big(\mathbb{I} + \mathbb{P}_i^0 (\mathbb{S}_i - \mathbb{S}_0)\big)^{-1} \Big) \Big(\sum_{i=1,n} \phi_i \big(\mathbb{I} + \mathbb{P}_i^0 (\mathbb{S}_i - \mathbb{S}_0)\big)^{-1} \Big)^{-1} \tag{1}$$

with the fourth order identity tensor $\mathbb{I}$, the stiffness tensors $\mathbb{S}_i$ and volume fractions ϕ_i of its constituents, as well as $\mathbb{P}_i^0 = \mathbb{R}_i \mathbb{S}_0^{-1}$, where $\mathbb{R}$ is the Eshelby tensor for the given inclusion problem [43] and $\mathbb{S}_0$ is a reference stiffness tensor that depends on the chosen homogenisation scheme [42, 44]. Following Reisinger et al. [45], the mineralised collagen fibril was modelled as a matrix-inclusion problem of oriented mineral spheroids in an isotropic collagen matrix, the extrafibrillar matrix as a continuous mineral matrix with spherical voids, and the extracellular matrix as cylindrical inclusions of mineralised collagen fibrils in a continuous isotropic extrafibrillar matrix (Fig. 2). In both cases, the Mori-Tanaka scheme was used with reference stiffness tensor $\mathbb{S}_0$ given by the matrix properties.

2.5.2. Axial splitting

Axial splitting of micropillars was modeled making use of an analytical solution of Ashby [46] for the formation of winglet cracks on an inclined flaw in a brittle matrix. Following the methodology of Östlund et al. [47], the mode 1 critical stress intensity factor $K_{1,c}$ for axial splitting along the middle of the pillar may be calculated. The critical stress intensity factor in this case is given by

$$K_{1,c} = \frac{1}{4} \sqrt{\frac{\pi}{tan\phi}} \cdot cos\phi \cdot cos(\frac{\pi}{2} - \phi) \cdot \sigma_{ult} \sqrt{d} \tag{2}$$

with the angle of the shear plane ϕ, the measured micropilalr ultimate stress σ_{ult}, and the pillar diameter d. In linear elastic fracture mechanics (LEFM), K_c is related to the critical energy release rate G_c by

$$G_c = \frac{K_c^2}{E}. \tag{3}$$

In this case, the relevant elastic modulus is $E_{t,ecm}$, the modulus of the ECM in the plane perpendicular to the fibre direction, which may be estimated using the continuum micromechanical model described above.

2.5.3. Fibril kinking

An analytical model for fibril kinking in uniaxial composites [48] was used for analysis of kink band formation. The model is based on the assumption that kink bands are caused by

matrix yielding rather than fibre buckling and start due to initial imperfections. It allows the prediction of the composite strength σ_{ult} based on the known extrafibrillar matrix (EFM) shear strength $\tau_{efm,ult}$, mineralised collagen fibre (MCF) diameter d_{mcf} and waviness (amplitude a, wavelength λ), fibril volume fraction ϕ_{mcf}, as well as the longitudinal fibril modulus $E_{33,mcf}$ and the extrafibrillar matrix shear modulus G_{efm} (for further details, see [48]). In this analysis, the model was used to compute the extrafibrilar mineral matrix shear strength from the measured uniaxial compressive strength of the micropillar:

$$\tau_{efm,ult} = \frac{\frac{1}{2}\pi a \lambda^2 A_{mcf} G_{efm,2d} \sigma_{ult}}{\frac{\lambda^2}{4}\phi_{mcf,2d} d_{mcf} G_{efm,2d} + \pi^2 \phi_{mcf,2d} E_{33,mcf} I_{mcf} - \frac{\lambda^2}{4} A_{mcf} \sigma_{ult}} \tag{4}$$

with $I_{mcf} = \frac{d_{mcf}^3}{12}$ and $A_{mcf} = d_{mcf}$ per unit thickness for the equivalent 2D problem. The longitudinal mineralised collagen fibre modulus $E_{33,mcf}$ and the extrafibrillar matrix shear modulus G_{efm} were estimated using the continuum micromechanics model described above [45]. Due to the large number of independent input parameters ($a, \lambda, d_{mcf}, G_{efm}, E_{33,mcf}, \phi_f, \sigma_{ult}$), a Gaussian error progression analysis with the assumption of random independent errors [49] was performed to get an estimate of the uncertainty in the modeling result.

3. Results

3.1. Mechanical testing

Microindentation of dry and hydrated ECM performed as part of an earlier study [28] demonstrated an influence of hydration and an anisotropy of micromechanical properties. The measured values for plain strain modulus and hardness (Tab. 1) are in accordance with values for human osteonal bone from the literature [19, 21] in the axial and transverse directions.

By measurements made on pre-test SEM images, micropillar diameter and aspect ratio were found to be 4.73 ± 0.13 µm (mean ± standard deviation) and 2.35 ± 0.24, respectively. The true stress-strain curves from the quasistatic micropillar compression of hydrated ECM are shown in Fig. 3. While the linear portion of the loading curve of the transverse pillars shows some scatter, they exhibit a good inter-experimental consistency in terms of yield and ultimate stress for both directions. Yield stress was found to be 0.171 ± 0.022 GPa in axial and 0.126 ± 0.025 GPa in transverse direction. Ultimate stress was 0.177 ± 0.021 GPa in axial and 0.169 ± 0.015 GPa in

transverse direction. The yield and ultimate properties for both directions under rehydrated as well as *in vacuo* [28] conditions are shown in Tab. 2.

The micropillars showed anisotropy in both yield properties and apparent hardening behaviour. The axial micropillars yielded at higher stresses compared to the transverse ones but showed less hardening, which is in line with *in vacuo* results [28]. As the pillars were compressed in load control, the apparent strain rate changed drastically after yielding. While the transverse pillars showed strain hardening accompanied by a moderate increase in strain rate, the axial pillars reached a distinct ultimate point only shortly after yield. As the load increase imposed by the loading protocol could not be supported after the ultimate point, the micropillars showed strain softening and deformed at drastically increased apparent strain rates up to $0.1s^{-1}$. Nevertheless, permanent deformation occurred rather than brittle failure, all micropillars showed a continuous unloading response.

3.2. Imaging

Based on SEM images taken after testing (Fig. 4), the main failure mode was found to be the development of one or more zones of localised shear deformation, similar to what was found *in vacuo* [28]. The main difference compared to dry conditions was that considerably higher strains were reached and that frequently more than one shear localisation developed. In micropillars where two sheared zones with opposing orientation met in the middle, a wedge was formed that subsequently led to an axial split.

BF-STEM and SAD were performed on untested control regions. BF-STEM showed a continuous fibrous structure with a strong texture along the osteon axis, mineral crystals were observed to follow the overall fibre direction. In regions of high ordering, the characteristic banding pattern with the 67 nm period of collagen was observed. In the SAD patterns, the (002) Bragg peak of hydroxyapatite was clearly visible and showed strong fiber texture with a relatively narrow orientation distribution, which was in line with the observed patterns in the STEM images. In the transverse sample, fibres were tilted with respect to the specimen direction. Fig. 5 shows BF-STEM images of undeformed regions oriented in the axial-radial plane of an osteon with both highly ordered regions showing the characteristic 67nm pattern as well as interstitial regions lacking this periodic contrast due to their disordered nature. Disordered regions were found in several TEM lamellae in between areas with high degree of allignment. A waviness of the fibrils was ob-

served in highly alligned areas. Measurements of the fiber waviness in the imaging plane revealed an amplitude a of 0.14 ± 0.04 µm and a wavelength of $\lambda = 1.73 \pm 0.39$ µm (n=19, Fig. 5). 2D Fast Fourier Transformations (FFT) on BF-STEM images of highly alligned areas with visible collagen banding revealed a fiber texture with a 67 nm period and an angular dispersion of $58 \pm 1.3^{\circ}$ representing the collagen fibrils (Fig. 5).

BF-STEM images of the compressed axial pillar revealed several deformation mechanisms of hydrated bone (Fig. 6) and their relation to the local microstructure. Fibrils were mostly aligned with the pillar axis and the characteristic 67 nm collagen banding pattern was visible. No significant influence zone of the focussed ion beam could be found, as mineral particles in diffraction condition and collagen banding were observed up to a thin layer of approximately 30 nm from the pillar walls. Material featuring a disordered, lacy microstructure was found in the rightmost region of the micropillar in BF-STEM (to the right of the dotted line in Fig. 6). SAD confirmed its disordered nature with the (002) Bragg peak showing an almost isotropic azimuthal distribution. A crack was observed to form at the interface between the ordered and the disordered regions and to protrude further into the micropillar. Furthermore, in two regions with fibrils highly aligned with the loading direction, regions of localised shear deformation were found which had been caused by the formation of kink bands. The mineralised collagen fibrils stayed continuous throughout the kink bands, even though kinking angles of $104 \pm 5^{\circ}$ (n=7) were observed, which were identical on the upper and lower boundary. Kink band thickness was measured to be in average 124 ± 13 nm (n=7). The angle with respect to the loading axis of the kink band as well as the crack on the right side of the pillar were approximately 54° . The formation of a kink band also led to large deformation of an isolated island of material in the top left corner of the micropillar. In this region, fibril buckling was observed, which was confirmed by a loss of fibre-texture in SAD patterns. It was found that the kink band starting at the top left corner and the crack from the interface of the ordered and disordered regions met in the middle of the pillar. This led to the formation of a wedge of material splitting the micropillar axially.

BF-STEM images of the deformed transverse pillar showed an overall homogeneous microstructure in the transverse direction (Fig. 7). A lacy structure was observed throughout the whole pillar and SAD patterns were characterised by a lack of (002) peaks. Tilting the sample by 15° led to a reappearance of the (002) peak in the SAD patterns (Fig. 7). Several shear cracks were found to emerge in regions where local fibril orientation was parallel to the emerging crack planes. Crack

tips were observed to arrest in regions where the local fibril orientation changed so that more fibrils were perpendicular to the crack plane.

3.3. Mechanical modeling

3.3.1. Axial splitting

It was observed on several axial micropillars that when two opposing kink bands or zones of localised shear deformation met inside the pillar, this could lead to the formation of a mode 1 crack splitting the pillar axially (Fig. 4 and 6). The mode 1 fracture toughness $K_{1,c}$ of bone extracelular matrix for the case of axial splitting of the ECM along fibril bundles was calculated using equation 2 (Fig. 2). For this analysis it was assumed that the splitting crack was formed at the ultimate stress. The critical stress intensity factor was thus estimated to be 0.07 MPa$\sqrt{m}$. Using the continuum micromechanical model described above to estimate the transverse ECM modulus as 16.6 GPa allowed to determine the critical energy release rate G_c based on LEFM (equation 3), which was found to be on the order of 0.3 Jm^{-2}.

3.3.2. Kink band formation

The fibre waviness was assessed based on STEM of undeformed areas and the amplitude and wavelength were found to be about 140 ± 40 nm and 1.73 µm, respectively. Fiber diameter was assumed to be 500 nm based on literature [51]. $E_{33,mcf}$ and G_{efm} were estimated using continuum micromechanics [45] and found to be 28.7 GPa and 12.8 GPa, respectively. Inserting these values into the analytical fibril kinking model (equation 4), an extrafibrillar matrix shear strength of approximately 120 MPa was calculated. Due to the large number of independent input parameters $(a, \lambda, d_{mcf}, G_{efm}, E_{33,mcf}, \phi_f, \sigma_{ult})$ an error analysis with the assumption of random independent errors [49] was performed. For ϕ_f, $E_{33,mcf}$, and G_{efm}, the standard errors were chosen following the experimental axial indentation modulus in wet condition to be 7%. For σ_{ult} the measured standard deviation of 13% for axial yield stress of micropillars under hydrated consitions was chosen. For fiber waviness, the measured standard deviations from STEM images on undeformed regions of approximately 25% were used, and for the fibril diameter a standard deviation of 20% was chosen. It was found that for these estimated standard errors, the uncertainty of the matrix shear strength calculated using the micromechanical model is approximately ±40 MPa.

4. Discussion

4.1. Mechanical testing

The reference microindentation measurements from an earlier study [28] were in agreement with other results for hydrated human osteonal bone [19, 21], confirming that ovine bone is indeed a reasonable model for human tissue at the ultrastructural level in hydrated condition [52]. Furthermore, they showed an influence of sample hydration and anisotropy of the ECM.

Micropillar compression under hydrated conditions showed some scatter in the linear region in the transverse direction. This was likely due to the presence of osteocyte lacunae and vascular porosity hidden under the surface at varying distances from the pillar base leading to an increased substrate heterogeneity. In the axial direction, the scatter in the linear region was much reduced, as blood vessels run normal to the surface and could be avoided more easily. A high consistency of the micropillar yield stress was found for both directions due to the relative homogeneity of ovine osteonal bone and good allignment between the sample and the indenter axis. Their variability were in the range reported for microindentation studies of hydrated bone [28, 21]. This is in line with earlier observations about the relative homogeneity of ECM properties in ovine bone [28, 53].

Due to the setup of the experiment in load control, the strain rate was only constant until yielding. In the plastic regime, the strain rate increased by several orders of magnitude up to $0.1\ \mathrm{s}^{-1}$, indicating incipient yielding. It is likely that the sample would have shown even more strain softening in displacement control and that in the case of load control it was partially stabilised by the rate-dependent nature of its post-yield behaviour. The resulting strain rates in the linear portion up to yield were in the same range as in a previous study – ($1 - 5 \cdot 10^{-4} s^{-1}$ compared to $5 \cdot 10^{-4} s^{-1}$ in [28]) – and may be regarded as quasi-static. Therefore a comparison of the apparent yield stresses is valid. The post-yield characteristics are dominated by the rate-dependent response and are representative of strain rates several orders of magnitude higher. However, it is interesting to note that similar to the earlier study [28], the axial micropillars yielded at higher stresses but showed much less hardening compared to the transverse ones. Axial pillars showed strain softening, while transverse ones hardened significantly, which is in line with [28] and hints at differences in the active deformation mechanisms.

The dimensions of the micropillars were chosen to be consistent with the average lamellar thickness of 3-7 µm and the tested volume of the microindentations following earlier work [28].

The aspect ratio of the micropillars were chosen so that a mostly uniaxial stress state would develop within the micropillar [29] while minimizing the risk of plastic buckling. The number of experiments was sufficient to show a clear anisotropy in the elastic regime by microindentation as well as for the yield behaviour at the extracellular matrix level by micropillar compression. It is noteworthy that the anisotropy ratio of the axial to the transverse yield stress was reduced from approximately 1.6 under vacuum conditions [28] to 1.3 under rehydrated conditions (see Tab. 2). This is in line with the reduced anisotropy ratio observed in the microindentation experiments between axial and transverse hardness from 1.5 in dry to 1.2 in rehydrated conditions [28] (see Tab. 1).

When comparing the yield behaviour of the microscopic compression experiments to macroscopic data from the literature, some differences were found. The response on the microlevel was plastic with very high maximum strains up to 35%, while macroscopic bone samples loaded uniaxially usually fail in a quasi-brittle fashion with the development and coalescence of microcracks and plastic strains below 1% [54, 36]. The uniaxial yield stresses of micropillars in the axial direction (0.17 ± 0.02 GPa) were 1.55 times higher than macroscopic values for hydrated tissue with a similar composition and microstructure from the literature (0.11 GPa for bovine bone in compression [36]). This is in line with the presence of size effects in quasi-brittle materials, which are known to behave in a less brittle manner and yield at higher stresses when smaller volumes are tested [55, 28]. However, the discrepancy was smaller compared to the factor of 2.4 found for strength under dry conditions [28]. For micropillar compression data under vacuum conditions [28], failure at moderate plastic strains of up to 8% was observed to be mostly due to the development of a single shear crack. In contrast, in this study several parallel zones of localised shear deformation were found on most of the micropillars. Also, experiments performed *in vacuo* showed yielding at 0.49 ± 0.10 GPa in the axial and 0.30 ± 0.02 GPa in the transverse directions, while the hydrated micropillars yielded at clearly reduced stresses (0.17 ± 0.02 GPa in the axial and 0.13 ± 0.03 GPa in the transverse directions). This discrepancy is in line with the reports of reduced hardness for microindentation in rehydrated tissue compared to the dry state [33, 28]. However, the reduction in properties of the micropillars of approximately 60% is considerably higher compared to what has been observed experimentally using microindentation (30-40%) [33, 28] in the past. This may be understood as follows: Firstly, the earlier micropillar compression experiments were performed *in vacuo*, while the dry microindentations were performed in air allowing more water

to remain inside the tissue compared to high vacuum conditions. Secondly, the rehydration of ECM greatly changes the viscous properties of the organic components of the ECM [5, 51, 35]. In microindentation, the predominant stress state under the indenter is multiaxial and has a large hydrostatic component, while the uniaxial micropillar compression features a higher portion of deviatoric stresses. Therefore, the effect of viscous flow on the latter test may be greater due to the decreased confinement and the increased ratio of deviatoric to hydrostatic portion of the predominant stress field.

The microscale yield properties reported in this study were in a similar range but slightly higher than values reported from previous studies based on microindentation [56]. These studies had to rely on assumptions regarding the nonlinear material behaviour and inverse methods to back-calculate material properties, while the data of the micropillar compressions may be interpreted in a relatively straightforward manner due to the mostly homogeneous, uniaxial stress state. Previous indentation studies suggested that a damage mechanism at the microscale might be responsible for some of the characteristics of indentation experiments in bone, such as a reduced unloading stiffness [57]. However, in an earlier micropillar study it was shown that the apparent modulus does not change as a function of plastic strain under uniaxial compressive loading, which is a strong indication that no diffuse cracks were developing inside the micropillars until failure and continuum damage mechanics is therefore not applicable. Due to the monotonic protocol used in this study, no further comment can be made on the possible reduction of modulus under hydrated conditions.

4.2. Imaging

BF-STEM and SAD analysis of axial and transverse micropillars as well as unloaded controls showed very interesting differences in the observed microstructure. In BF-STEM, which is characterised by a combination of mass-thickness and diffraction contrast, mineral particles appear dark, as they are crystalline and the heaviest scatterers in the composite material bone. BF-STEM and SAD of the untested controls revealed a continuous fibrous structure with the 67 nm banding characteristic of collagen and apatite crystals following the fibrous texture (Fig. 5). The main orientation could be observed based on the (002) and (004) Bragg peaks of the apatite crystals in the SAD patterns. The axial control sample showed a high degree of alignment with respect to the loading direction and little dispersion, while the transverse control sample showed a considerably

higher mean angle with respect to the loading direction and a stronger dispersion. Disordered regions were found between highly ordered areas in several TEM lamellae, which is in line with findings of Reznikov et al. [50]. In regions with a high degree of alignment, the characteristic banding pattern with the 67 nm period of collagen was clearly visible and a waviness of the fibrils was observed. Measurement of the fiber waviness in the imaging plane revealed an amplitude a of 0.14 ± 0.04 µm and a wavelength of $\lambda = 1.73 \pm 0.39$ µm. 2D FFT of highly alligned areas with visible collagen banding showed a partial ring representing the 67 nm collagen banding with an angular dispersion of $58 \pm 1.3^{\circ}$ ($n = 4$). When considering the image as an array of parallel, wavy fibers described by a sinus function $f(x) = a \cdot sin(\frac{2\pi x}{\lambda})$, the maximum angle is expected to occur at $x = 0$ and $x = n\lambda/2$. Using this, the angular dispersion may be predicted based on the waviness using $2\theta_{max} = 2tan^{-1}(\frac{2\pi a}{\lambda})$. Inserting the measurements of amplitude and wavelength into this equation, an angular dispersion of 54° is predicted, which is highly consistent with the FFT results. This means that fibril waviness alone may account for a large portion of the fibril dispersion and further corroborates the waviness measurements. However, it has to be noted that here a possibly three dimensional waviness was measured in one plane only, which means that the values reported here are likely lower bounds.

BF-STEM of the compressed axial pillar revealed the active microscale deformation mechanisms of hydrated lamellar bone and their relation to the observed microstructure (Fig. 6): Large parts of the pillar featured fibrils oriented in the loading direction, the visibility of the 67 nm collagen banding pattern suggests a high degree of alignment of the mineralised collagen fibrils. The fact that mineral particles in diffraction condition and collagen banding were observed up to 30 nm from the micropillar walls suggests that the Ga^{+} ion influence zone is negligibly small compared to the pillar dimensions, which is in line with earlier Monte Carlo simulations [28]. Disordered structures like the one found in the rightmost region of the axial micropillar were also found in several of the untested control regions and are in line with reports of unordered interlayers between adjacent laminae in the literature [50]. SAD confirmed the disordered nature of the lacy structure with the (002) Bragg peak showing an almost isotropic azimuthal distribution, while a strong fibre texture was observed in the ordered regions.

The observed deformation mechanisms included a crack formed at the interface between the ordered and the disordered regions, kink band formation in regions where fibrils were strongly aligned with the loading direction, and mode 1 axial splitting. This is in agreement with the

observed softening behaviour of axial micropillars, as both kink band and crack formation lead to load drops. Unlike in engineering composites, where reinforcing fibres tend to break at the edges of a kink band [58], the mineralised collagen fibrils stayed continuous, even though very high kinking angles were observed. This emphasises the high degree of ductility of mineralised collagen fibrils. The fact that kink angles on the upper and lower boundary of the bands were approximately identical suggests that kink bands were formed by pure shear deformation and that no volume change took place [59]. The angle of the kink band and the crack on the right side of the pillar were in line with values reported in the literature for epoxy-based engineering composites [60]. Both the crack (dashed line, Fig. 6) and the kink band (dot-dashed line, Fig. 6) could be traced back to the presence of preexisting defects, in the case of the crack an interface between regions with different fibril orientation, and in the case of the kink band a pore of approximately 50 nm diameter. The development of localised kink bands under compressive loading due to the presence of flaws is a known phenomenon described in the composites literature [59, 58], it has not however been observed in bone so far. The kink band starting at the top left corner and the crack from the interface of the ordered and disordered regions met approximately in the middle of the pillar leading to the formation of a wedge of material, which split the micropillar axially with a mode 1 crack. This phenomenon is known from other brittle materials such as GaAs, where pillars split axially when 2 opposing shear planes meet in the pillar center [27].

BF- images of the deformed transverse pillar showed an overall homogeneous microstructure in the transverse direction (Fig. 7). A lacy structure observed throughout the whole transverse pillar (Fig. 7) was interpreted as cross sections of fibrils oriented out of the sample plane surrounded by extrafibrillar mineral, in line with the reports of McNally et al [61]. Supporting this, it was observed that SAD patterns in the transverse pillar were characterised by a lack of (002) and (004) peaks. This was caused by the majority mineral crystals being oriented perpendicular to the imaging plane, therefore the basal planes causing the (002) Bragg peaks were not in diffraction condition. This interpretation could be confirmed by tilting the sample by 15°, which led to a reappearance of the (002) and (004) peaks in the SAD patterns (Fig. 7). Several shear cracks were found to emerge in regions where local fibril orientation was parallel to the emerging crack planes. This lead to a minimum number of fibrils bridging the crack, thereby minimising the local fracture toughness. Crack tips were observed to arrest in regions where the local fibril orientation changed so that further crack growth was hindered by an increased number of bridging fibrils. These

findings are in line with observations made by HRSEM in an earlier study under non-hydrated conditions [28].

4.3. Mechanical Modeling

4.3.1. Axial splitting

It was observed on several axial micropillars that when two opposing kink bands or zones of localised shear deformation met inside the pillar, this could lead to the formation of a mode 1 crack splitting the pillar axially (Fig. 2 and 7). This phenomenon is known for compressive failure of brittle materials [46, 47]. It is assumed that the splitting crack formed at the ultimate stress, in line with the observation that crack propagation leads to load drops in displacement controlled experiments [47]. The use of LEFM is justified by the small difference between apparent yield and ultimate point (Tab. 2), the pronounced strain softening observed in the axial pillars (Fig. 4), and the alignment of the crack with the fibril direction (Fig. 2) which suggest that little plastic deformation took place at the crack tip. The critical stress intensity factor was found to be $0.07\,\mathrm{MPa}\sqrt{m}$ using equation 2. In LEFM, the critical energy release rate G_c may be estimated if K_c and $E_{t,ecm}$, the moduluis of the ECM in the plane perpendicular to the fibre direction, are known (equation 3). $E_{t,ecm}$ was estimated using continuum micromechanics to be 16.6 GPa using the above described model for bone ECM [45], which is well in line with the nanoindentation results (Tab. 1). Using this, the critical energy release rate is estimated to be in the order of $0.3\,\mathrm{Jm}^{-2}$. The critical stress intensity factor identified here is in the range of elastomers and foams, however the relatively high elastic modulus of the ECM places it near the theoretical lower bound for K_c/E of $4.5 \cdot 10^{-6}\ \sqrt{m}$ [62] similar to brittle engineering ceramics. The microscale fracture toughness of lamellar bone for splitting along the fibre direction reported here is also 1-2 orders of magnitude smaller than what has been reported in the literature for macroscopic cortical bone ($3 - 10\,\mathrm{MPa}\sqrt{m}$, [15, 17]). This is likely caused by the absence of extrinsic toughening mechanisms (crack deflection and twisting at interfaces, constrained microcracking, uncracked ligament bridging [15, 17]) in the micropillar, which showed a highly aligned microstructure in the region of the axial crack. The observed micropillar splitting is therefore governed by decohesion between mineralised collagen fibrils and thus the fracture toughness of the porous extrafibrillar matrix is relevant and no higher scale toughening mechanisms are active. The estimated toughness is in line with values for wet polycrystalline hydroxyapatite ($0.4\,\mathrm{MPa}\sqrt{m}$ for 25% porosity, [63])

when taking into account the increased porosity in the extrafibrillar matrix (33-55%, [64, 45]). This analysis only provides an order of magnitude estimate, due to the various modelling assumptions and idealisations. However, it provides means to evaluate the fracture toughness of small volumes of hydrated bone ECM when splitting them along the fibril direction, without the influence of higher scale toughening mechanisms [14, 15, 16, 17]. The result clearly underlines the importance of bone's hierarchical microstructure for its fracture resistance, as larger specimens show considerable higher toughness due to the presence of multiscale toughening mechanisms. There is a need for further dedicated fracture toughness measurements of hydrated bone samples on this length scale to further corroborate this first estimate.

4.3.2. Kink band formation

As kink band formation was observed in axial micropillars, which is one possible cause for the observed apparent softening behaviour [48], a mechanical analysis was performed using an analytical model for fibril kinking in uniaxial composites [48]. It is assumed that kink bands are caused by matrix yielding rather than fibril buckling and start due to initial imperfections, the interface between matrix and fibers stays intact. In this study, the model was inverted to estimate the matrix shear strength from the measured uniaxial compressive strength of the micropillar (equation 4). Fiber diameter was assumed to be 500 nm based on literature [51]. The longitudinal mineralised collagen fibre modulus $E_{33,mcf}$ and the extrafibrillar matrix shear modulus G_{efm} were estimated using continuum micromechanics [45] and found to be 28.7 GPa and 12.8 GPa, respectively. While collagen should ideally be considered as transversely isotropic, the effect of modeling it as an isotropic matrix in the mineralized fibril to reduce model complexity [45] is minor when looking at axial properties, as the homogenized stiffness is dominated by the oriented mineral platelets. Using the analytical fibril kinking model (equation 4), an extrafibrillar matrix shear strength of approximately 120 MPa was estimated. In earlier work of Gupta et al. [9] based on interpretation of in-situ SAXS measurements during tensile testing of parallel-fibred bone, it was postulated that inelastic deformation in bone is characterized by an interface failure between the EFM and the MCF. Using a stick-slip model, they arrived at a critical shear strength of the interface of 600 MPa, which is considerably higher than what we report here. The reason for this discrepancy lies in the different concepts for nanoscale plasticity, as we assumed that the matrix-fibril interface remains intact and that plastic flow is happening within the EFM itself.

Which mechanisms exactly act at the nanoscale is not entirely clear at the moment and further studies on this topic are needed. Due to the large number of independent input parameters in the kinking analysis ($a, \lambda, d_{mcf}, G_{efm}, E_{33,mcf}, \phi_f, \sigma_{ult}$), a Gaussian error progression analysis with the assumption of random independent errors [49] was performed. For ϕ_f, $E_{33,mcf}$, and G_{efm}, which are either elastic properties or closely linked to them, the standard errors were chosen following the measured axial indentation modulus in wet condition to be 7%. For σ_{ult} the measured standard deviation of 13% for axial ultimate stress of micropillars under hydrated conditions was chosen. For the fiber waviness, the measured standard deviations from STEM images on undeformed regions of approximately 25% were used, and for the fibril diameter a standard deviation of 20% was chosen based on the relatively large range of values reported in the literature ($50 - 500$ nm, [64, 17, 51]). It was found that under these assumptions the uncertainty of the matrix shear strength is approximately ± 40 MPa. Albeit only a rough estimate, this analysis sheds light on the shear strength of hydrated extrafibrillar matrix by analysis of fibril kinking observed in a microscale experiment with defined uniaxial boundary conditions. Further research is needed to measure the EFM shear strength with improved precision.

4.4. Conclusion

An experimental study was undertaken to assess the yield and failure properties of bone extracellular matrix on the length scale of a single lamella under uniaxial loading and rehydrated conditions. Micropillar compression was combined with post-test TEM observation and micromechanical modelling. Microscale yield stresses (0.17 GPa in axial, 0.13 GPa in transverse directions) were found to be increased by a factor of 1.55 compared to the macroscale [36] and very high inelastic strains up to 30% could be reached without catastrophic failure. While microscale ECM samples show an apparent ductile response and deform homogeneously until the development of zones of localised shear deformation, in the form of kink bands or shear cracks, the macroscopic response is quasi-brittle with microcracks forming and coalescing even at small global strains, leading to catastrophic failure [28, 36]. Hydration was shown to have a major influence on the microscale yield properties with a reduction by 60% compared to vacuum conditions [28]. This is in line with the reduction of microindentation properties upon rehydration of bone tissue [33, 28] and is most likely explained by drastic changes in the mechanical behaviour of collagen in the presence of water [51, 35]. Discrepancies in magnitude of the reduction may be attributed to the reduced

confinement and thus increased deviatoric loading conditions compared to microindentation. The anisotropy of the yield properties of the micropillars was shown to reduce upon rehydration, which is in line with the change in anisotropy of microindentation hardness [28]. Finally, TEM analysis of compressed micropillars revealed anisotropic deformation and failure mechanisms in lamellar bone: Axial micropillars failed by formation of kink bands or cracks in the presence of nanoscale defects as well as axial splitting, while transverse pillars showed shear cracking in regions with unfavourable fibril orientations. Analysis of the failure mechanisms in the axial pillar combining analytical models for fibril kinking and axial splitting with a continuum mechanical description of the ECM allowed an estimation of the shear strength of the extrafibrillar matrix to be made: 120 ± 40 MPa, as well as the mode 1 critical stress intensity factor of the extracellular matrix: $0.07\ \mathrm{MPa}\sqrt{m}$, which corresponds to a critical energy release rate of $0.3\ \mathrm{Jm}^{-2}$. Bone therefore shows a high apparent ductility on the microscale while at the same time featuring a very low fracture toughness for splitting along the fibril direction. This means that even when fibril bundles separate, this does not necessarily lead to a catastrophic failure of the overall structure under compression. The microscale fracture toughness is 1-2 orders of magnitude smaller than values reported for macroscopic bone [17], which may be rationalised by the absence of extrinsic toughening mechanisms when testing small volumes of bone with a primarily uniaxial fibril orientation. These result clearly underline the importance of bone's hierarchical microstructure for its macroscopic strength and fracture resistance and the need to study structure-property relationships and failure mechanisms under hydrated conditions on all length scales. The insight gained from this work can help to develop micromechanical models of bone inelastic deformation that could be used to enrich existing finite element codes for fracture risk prediction in a clinical setting in the future.

5. Author Contributions

The study was planned by JS, UW, PZ, and JM. The experimental setup was developed by JS and UW. Micropillars were fabricated and tested by JS. TEM lamellae were prepared and imaged by AT and DC. Micromechanical modeling was performed by JS. The data was interpreted and the manuscript written by JS with contributions of all coauthors. All authors have read and approved the final manuscript.

6. Competing financial interests

The authors declare no competing financial interests.

[1] S. Weiner, W. Traub, H. Wagner, Lamellar bone: Structure-function relations, Journal of Structural Biology 126 (3) (1999) 241 – 255.

[2] P. Fratzl, R. Weinkamer, Nature's hierarchical materials, Progress in Materials Science 52 (8) (2007) 1263 – 1334.

[3] S. Lees, N.-J. Tao, S. Lindsay, Studies of compact hard tissues and collagen by means of brillouin light scattering, Connective Tissue Research 24 (3-4) (1990) 187–205.

[4] M. Giraud-Guille, Twisted plywood architecture of collagen fibrils in human compact bone osteons, Calcified tissue international 42 (3) (1988) 167–180.

[5] J. D. Currey, Bones: Structure and Mechanics, Princeton University Press, 2002.

[6] U. Wolfram, J. Schwiedrzik, Post-yield and failure properties of cortical bone, BoneKEy Reports 5.

[7] G. C. Reilly, J. D. Currey, The development of microcracking and failure in bone depends on the loading mode to which it is adapted, Journal of Experimental Biology 202 (5) (1999) 543–552.

[8] F. J. O'Brien, D. Taylor, T. C. Lee, An improved labelling technique for monitoring microcrack growth in compact bone, Journal of Biomechanics 35 (4) (2002) 523 – 526.

[9] H. S. Gupta, J. Seto, W. Wagermaier, P. Zaslansky, P. Boesecke, P. Fratzl, Cooperative deformation of mineral and collagen in bone at the nanoscale., Proceedings of the National Academy of Sciences 103 (47) (2006) 17741–17746.

[10] H. Gupta, W. Wagermaier, G. Zickler, J. Hartmann, S. Funari, P. Roschger, H. Wagner, P. Fratzl, Fibrillar level fracture in bone beyond the yield point, International Journal of Fracture 139 (2006) 425–436.

[11] H. S. Gupta, P. Fratzl, M. Kerschnitzki, G. Benecke, W. Wagermaier, H. O. Kirchner, Evidence for an elementary process in bone plasticity with an activation enthalpy of 1 eV, Journal of The Royal Society Interface 4 (13) (2007) 277–282.

[12] G. E. Fantner, T. Hassenkam, J. H. Kindt, J. C. Weaver, H. Birkedal, L. Pechenik, J. A. Cutroni, G. A. Cidade, G. D. Stucky, D. E. Morse, P. K. Hansma, Sacrificial bonds and hidden length dissipate energy as mineralized fibrils separate during bone fracture., Nature Materials 4 (8) (2005) 612–616.

[13] G. E. Fantner, J. Adams, P. Turner, P. J. Thurner, L. W. Fisher, P. K. Hansma, Nanoscale ion mediated networks in bone: osteopontin can repeatedly dissipate large amounts of energy, Nano Letters 7 (8) (2007) 2491–2498.

[14] D. Vashishth, J. Behiri, W. Bonfield, Crack growth resistance in cortical bone: concept of microcrack toughening, Journal of biomechanics 30 (8) (1997) 763–769.

[15] R. K. Nalla, J. H. Kinney, R. O. Ritchie, Mechanistic fracture criteria for the failure of human cortical bone, Nature materials 2 (3) (2003) 164–168.

[16] H. Gupta, P. Zioupos, Fracture of bone tissue: The hows and the whys, Medical Engineering & Physics 30 (10) (2008) 1209 – 1226.

[17] R. O. Ritchie, M. J. Buehler, P. Hansma, Plasticity and toughness in bone, Physics Today 62 (6).

[18] J.-Y. Rho, T. Y. Tsui, G. M. Pharr, Elastic properties of human cortical and trabecular lamellar bone measured by nanoindentation, Biomaterials 18 (20) (1997) 1325–1330.

[19] P. K. Zysset, X. Edward Guo, C. Edward Hoffler, K. E. Moore, S. A. Goldstein, Elastic modulus and hardness of cortical and trabecular bone lamellae measured by nanoindentation in the human femur, Journal of Biomechanics 32 (10) (1999) 1005–1012.

[20] N. Rodriguez-Florez, M. L. Oyen, S. J. Shefelbine, Insight into differences in nanoindentation properties of bone., Journal of the Mechanical Behavior of Biomedical Materials 18 (2013) 90–99.

[21] M. Mirzaali, J. J. Schwiedrzik, S. Thaiwichai, P. K. Zysset, U. Wolfram, Mechanical properties of cortical bone and their relationships with age, gender, composition and microindentation properties in the elderly, Bone 93 (2016) 196–211.

[22] W. C. Oliver, G. M. Pharr, An improved technique for determining hardness and elastic modulus using load and displacement sensing indentation experiments, Journal of Materials Research 7 (06) (1992) 1564–1583.

[23] A. Fischer-Cripps, Nanoindentation, Springer, New York, 2002.

[24] X. Chen, N. Ogasawara, M. Zhao, N. Chiba, On the uniqueness of measuring elastoplastic properties from indentation: The indistinguishable mystical materials, Journal of the Mechanics and Physics of Solids 55 (8) (2007) 1618 – 1660.

[25] J. J. Schwiedrzik, P. K. Zysset, The influence of yield surface shape and damage in the depth-dependent response of bone tissue to nanoindentation using spherical and berkovich indenters, Computer Methods in Biomechanics and Biomedical Engineering 18 (5) (2015) 492–505.

[26] M. D. Uchic, D. M. Dimiduk, A methodology to investigate size scale effects in crystalline plasticity using uniaxial compression testing, Materials Science and Engineering: A 400 (2005) 268–278.

[27] P. R. Howie, S. Korte, W. J. Clegg, Fracture modes in micropillar compression of brittle crystals, Journal of Materials Research 27 (1) (2012) 141–151.

[28] J. Schwiedrzik, R. Raghavan, A. Bürki, V. LeNader, U. Wolfram, J. Michler, P. Zysset, In situ micropillar compression reveals superior strength and ductility but an absence of damage in lamellar bone, Nature Materials 13 (7) (2014) 740–747.

[29] X. Maeder, W. Mook, C. Niederberger, J. Michler, Quantitative stress/strain mapping during micropillar compression, Philosophical Magazine 91 (7-9) (2011) 1097–1107.

[30] K. W. Luczynski, A. Steiger-Thirsfeld, J. Bernardi, J. Eberhardsteiner, C. Hellmich, Extracellular bone matrix exhibits hardening elastoplasticity and more than double cortical strength: evidence from homogeneous compression of non-tapered single micron-sized pillars welded to a rigid substrate, Journal of the mechanical behavior of biomedical materials 52 (2015) 51–62.

[31] O. A. Tertuliano, J. R. Greer, The nanocomposite nature of bone drives its strength and damage resistance, Nat Mater 15 (11) (2016) 1195–1202.

[32] J. S. Nyman, A. Roy, X. Shen, R. L. Acuna, J. H. Tyler, X. Wang, The influence of water removal on the strength and toughness of cortical bone, Journal of Biomechanics 39 (5) (2006) 931 – 938.

[33] U. Wolfram, H.-J. Wilke, P. K. Zysset, Rehydration of vertebral trabecular bone: influences on its anisotropy, its stiffness and the indentation work with a view to age, gender and vertebral level, Bone 46 (2) (2010) 348–354.

[34] M. Unal, O. Akkus, Raman spectral classification of mineral- and collagen-bound water's associations to elastic and post-yield mechanical properties of cortical bone, Bone 81 (2015) 315 – 326.

[35] A. Masic, L. Bertinetti, R. Schuetz, S.-W. Chang, T. H. Metzger, M. J. Buehler, P. Fratzl, Osmotic pressure induced tensile forces in tendon collagen, Nature Communications 6.

[36] M. J. Mirzaali, A. Bürki, J. Schwiedrzik, P. K. Zysset, U. Wolfram, Continuum damage interactions between tension and compression in osteonal bone, Journal of the Mechanical Behavior of Biomedical Materials 49, 355–369.

[37] J. F. Ziegler, J. P. Biersack, The stopping and range of ions in matter, Springer, New York, 1985.

[38] H. Zhang, B. E. Schuster, Q. Wei, K. T. Ramesh, The design of accurate micro-compression experiments, Scripta Materialia 54 (2) (2006) 181–186.

[39] I. N. Sneddon, The relation between load and penetration in the axisymmetric boussinesq problem for a punch of arbitrary profile, International Journal of Engineering Science 3 (1) (1965) 47–57.

[40] M. Ashby, D. Jones, Engineering Materials, Pergamon Press, Oxford, 1980.

[41] R Development Core Team, R: A Language and Environment for Statistical Computing, R Foundation for Statistical Computing, Vienna, Austria, ISBN 3-900051-07-0 (2008).

[42] S. Nemat-Nasser, M. Hori, Micromechanics: Overall properties of heterogeneous materials, Elsevier, Amsterdam, 1993.

[43] J. D. Eshelby, The determination of the elastic field of an ellipsoidal inclusion, and related problems, Proceedings of the Royal Society of London. Series A. Mathematical and Physical Sciences 241 (1226) (1957) 376–396.

[44] A. Zaoui, Continuum micromechanics: A survey, Journal of Engineering Mechanics 128 (8) (2002) 808–816.

[45] A. Reisinger, D. Pahr, P. Zysset, Sensitivity analysis and parametric study of elastic properties of an unidirectional mineralized bone fibril-array using mean field methods, Biomechanics and Modeling in Mechanobiology 9 (2010) 499–510.

[46] M. Ashby, S. Hallam, The failure of brittle solids containing small cracks under compressive stress states, Acta Metallurgica 34 (3) (1986) 497 – 510.

[47] F. Östlund, P. R. Howie, R. Ghisleni, S. Korte, K. Leifer, W. J. Clegg, J. Michler, Ductile–brittle transition in micropillar compression of gaas at room temperature, Philosophical Magazine 91 (7-9) (2011) 1190–1199.

[48] S. Pimenta, R. Gutkin, S. Pinho, P. Robinson, A micromechanical model for kink-band formation: Part iianalytical modelling, Composites Science and Technology 69 (78) (2009) 956 – 964.

[49] J. Taylor, An introduction to error analysis, University Science Books, Sausalito, 1982.

[50] N. Reznikov, R. Shahar, S. Weiner, Bone hierarchical structure in three dimensions, Acta Biomaterialia 10 (9) (2014) 3815 – 3826.

[51] A. K. Nair, A. Gautieri, S.-W. Chang, M. J. Buehler, Molecular mechanics of mineralized collagen fibrils in bone, Nature Communications 4 (2013) 1724.

[52] A. Pearce, R. Richards, S. Milz, E. Schneider, S. Pearce, Animal models for implant biomaterial research in bone: a review, European Cells & Materials 13 (2007) 1–10.

[53] J. Schwiedrzik, P. Zysset, Quantitative analysis of imprint shape and its relation to mechanical properties measured by microindentation in bone, Journal of Biomechanics 48 (2015) 210–216.

[54] D. T. Reilly, A. H. Burstein, The elastic and ultimate properties of compact bone tissue, Journal of Biomechanics 8 (6) (1975) 393 – 405.

[55] Z. P. Bažant, Scaling theory for quasibrittle structural failure, Proceedings of the National Academy of Sciences of the United States of America 101 (37) (2004) 13400–13407.

[56] D. Carnelli, D. Gastaldi, V. Sassi, R. Contro, C. Ortiz, P. Vena, A finite element model for direction-dependent mechanical response to nanoindentation of cortical bone allowing for anisotropic post-yield behavior of the tissue, Journal of biomechanical engineering 132 (8) (2010) 081008.

[57] J. Zhang, M. M. Michalenko, E. Kuhl, T. C. Ovaert, Characterization of indentation response and stiffness reduction of bone using a continuum damage model, Journal of the Mechanical Behavior of Biomedical Materials 3 (2) (2010) 189–202.

[58] C. Schultheisz, A. Waas, Compressive failure of composites, part i: Testing and micromechanical theories, Progress in Aerospace Sciences 32 (1996) 1–42.

[59] C. R. Chaplin, Compressive fracture in unidirectional glass-reinforced plastics, Journal of Materials Science 12 (1977) 347–352.

[60] H. T. Hahn, M. M. Sohi, Buckling of a fiber bundle embedded in epoxy, Composites Science and Technology 27 (1986) 25–41.

[61] E. McNally, F. Nan, G. A. Botton, H. P. Schwarcz, Scanning transmission electron microscopic tomography of cortical bone using z-contrast imaging, Micron 49 (2013) 46 – 53.

[62] M. Ashby, Mapping the fracture properties of engineering materials, Philosophical Magazine 93 (28-30) (2013) 3878–3892.

[63] G. De With, H. J. A. Van Dijk, N. Hattu, K. Prijs, Preparation, microstructure and mechanical properties of dense polycrystalline hydroxy apatite, Journal of Materials Science 16 (6) (1981) 1592–1598.

[64] A. Fritsch, C. Hellmich, Universal microstructural patterns in cortical and trabecular, extracellular and extravascular bone materials: Micromechanics-based prediction of anisotropic elasticity, Journal of Theoretical Biology 244 (4) (2007) 597–620.

Table 1: Mean ± standard deviation of plain strain modulus E^* and indentation hardness H_{IT} for microindentations in the axial and transverse directions in dry and rehydrated conditions [28].

Direction	Condition	E^*/GPa	H_{IT}/GPa	n
Axial	Air dried	27.5 ± 2.2	1.01 ± 0.13	50
Transv.	Air dried	19.0 ± 1.8	0.67 ± 0.08	72
Axial	Rehydr.	22.8 ± 1.6	0.60 ± 0.11	67
Transv.	Rehydr.	14.5 ± 1.6	0.51 ± 0.08	83

Table 2: Mean ± standard deviation of yield stress σ_y and ultimate stress σ_{ult} in GPa as well as qualitative description of postyield behaviour and failure patterns of quasistatic monotonic micropillar compressions in axial and transverse directions for rehydrated conditions or *in vacuo* [28].

Direction	Condition	σ_y/GPa	σ_{ult}/GPa	N	Postyield	Dominant failure pattern
Axial	In vacuo	0.49 ± 0.1	0.75 ± 0.06	19	Softening	Localized shear crack or split
Transv.	In vacuo	0.3 ± 0.02	0.59 ± 0.04	20	Hardening	Localized shear crack
Axial	Rehydrated	0.17 ± 0.022	0.18 ± 0.021	11	Softening	Several sheared bands or split
Transv.	Rehydrated	0.13 ± 0.025	0.17 ± 0.015	9	Hardening	Several sheared bands

Figure 1: Sketch of the rehydrated micropillar compression setup. Samples are rehydrated for 2h in HBSS. Just before starting the experiment, excess HBSS on the specimen surface is removed leaving the micropillar submerged in HBSS inside the FIB trench during monotonic compression.

Figure 2: Top: Schematics depicting the hierarchical micromechanical model of bone extracellular matrix (ECM) following [45] consisting of mineralised collagen fibrils (MCF) and extrafibrillar matrix (EFM). EFM is modelled as a porous mineral foam, MCF as spheroidal mineral inclusions in an isotropic collagen matrix. Bottom: Modelled failure mechanisms in axial micropillars, i.e. axial splitting of the micropillar where opposing zones of localised shear deformation meet [47] and kink band formation [48].

Figure 3: True axial stress σ vs. true axial strain lnU_{33} of monotonic micropillar compressions in a) axial and b) transverse direction under hydrated conditions. Axial pillars yield at higher stresses, but show strain softening. Transverse pillars yield at lower stresses and show a pronounced strain hardening up to ultimate stresses comparable to the axial pillars. Loading moduli are indicated by dashed lines, yield points by hollow circles and ultimate points by full circles.

Figure 4: HRSEM images of axial (top) and transverse (bottom) micropillars taken after monotonic compression showing failure by the development of zones of localised shear deformation (black arrows) and axial splitting. Pillars a1, c1 and b2 were used for further TEM analysis. Scale bars represent 2µm.

Figure 5: Top: a1-c1) BF-STEM images of undeformed bone in the axial-radial plane of an osteon showing highly ordered regions with the characteristic 67 nm collagen banding pattern as well as interstitial disordered regions lacking this periodic contrast. Individual fibrils on which waviness amplitude a and wavelength λ were measured are highlighted by dashed lines. Interfaces between ordered and disordered regions are marked by dotted lines. Bottom: a2-c2) 2D FFTs of ordered subregions showing ring fragments of structures with a 67 nm period identified as the collagen banding with an angular dispersion 2θ of $58 \pm 1.3^{\circ}$(n=4). Scale bars represent 1µm.

Figure 6: BF-STEM images and SAD patterns of a compressed axial micropillar. a) BF-STEM overview of the whole micropillar showing regions with a highly aligned fibre texture and disordered regions; the dotted line marks the boundary between the two regions, dashed lines mark observed cracks and dot-dashed lines kink bands. b) BF-STEM of the upper right corner showing a kink band as well as crack formation at the interface between the ordered and unordered regions (kink band denoted by white arrows, crack by black arrows), c) BF-STEM of the crack splitting the micropillar axially, d) SAD pattern of a highly deformed region in the upper left corner showing fibril buckling and kinking demonstrating the loss of fibre texture, e) SAD pattern in the ordered region showing the high degree of alignment of the mineral crystals with the loading direction, f) SAD pattern of the disordered region showing a near isotropic orientation of mineral. Scale bars represent 500nm. The missing lower left corner of the micropillar is an artefact of the TEM lamella preparation.

Figure 7: BF-STEM images and SAD patterns of a compressed transverse micropillar. a) BF-STEM overview of the whole micropillar showing a homogeneous lacy microstructure due to fibres oriented perpendicular to the imaging plane, b) to d) BF-STEM images of cracks formed in regions with an adverse fibril orientation (fibril orientation highlighted by full white lines, cracks by black dashed lines), e) SAD pattern showing an absence of (002) and (004) Bragg peaks, f) tilting the sample 15° leads to a reappearance of the (002) and (004) peaks suggesting mineral platelets are oriented mainly perpendicular to the image plane. Scale bars represent 500nm.

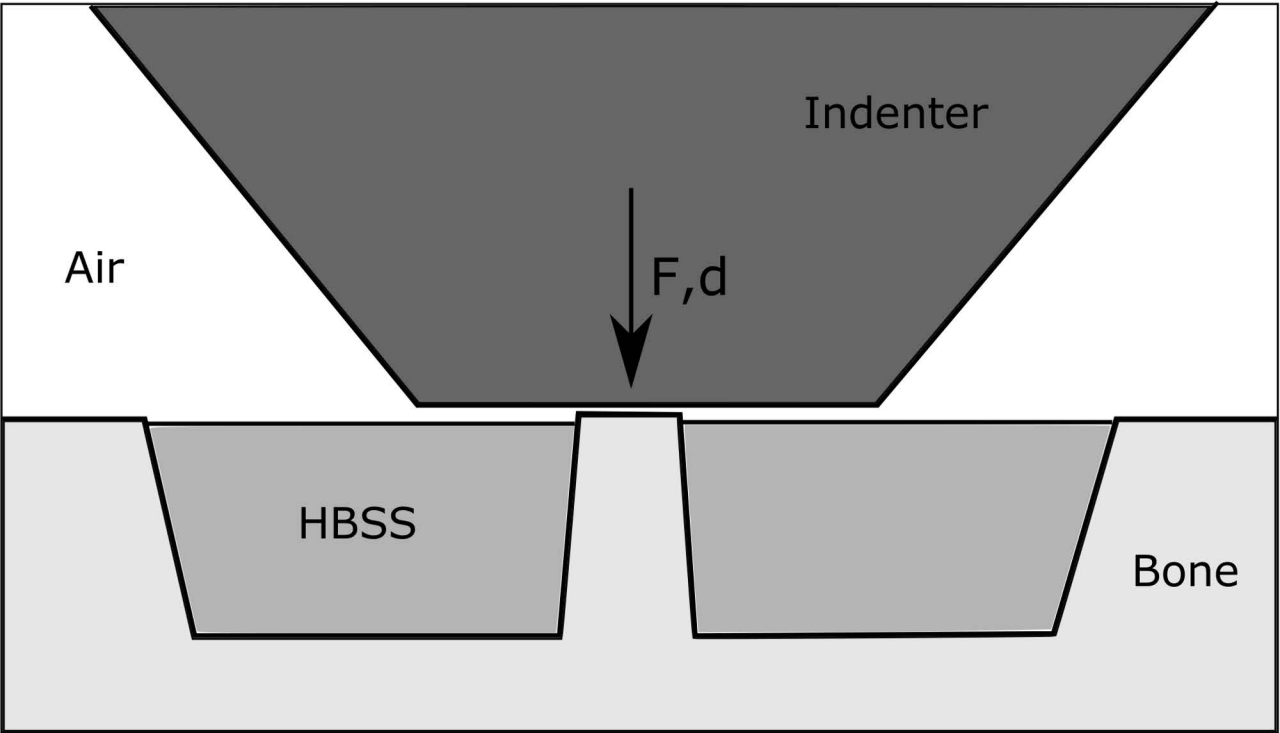
Indenter
Air
F,d
HBSS
Bone

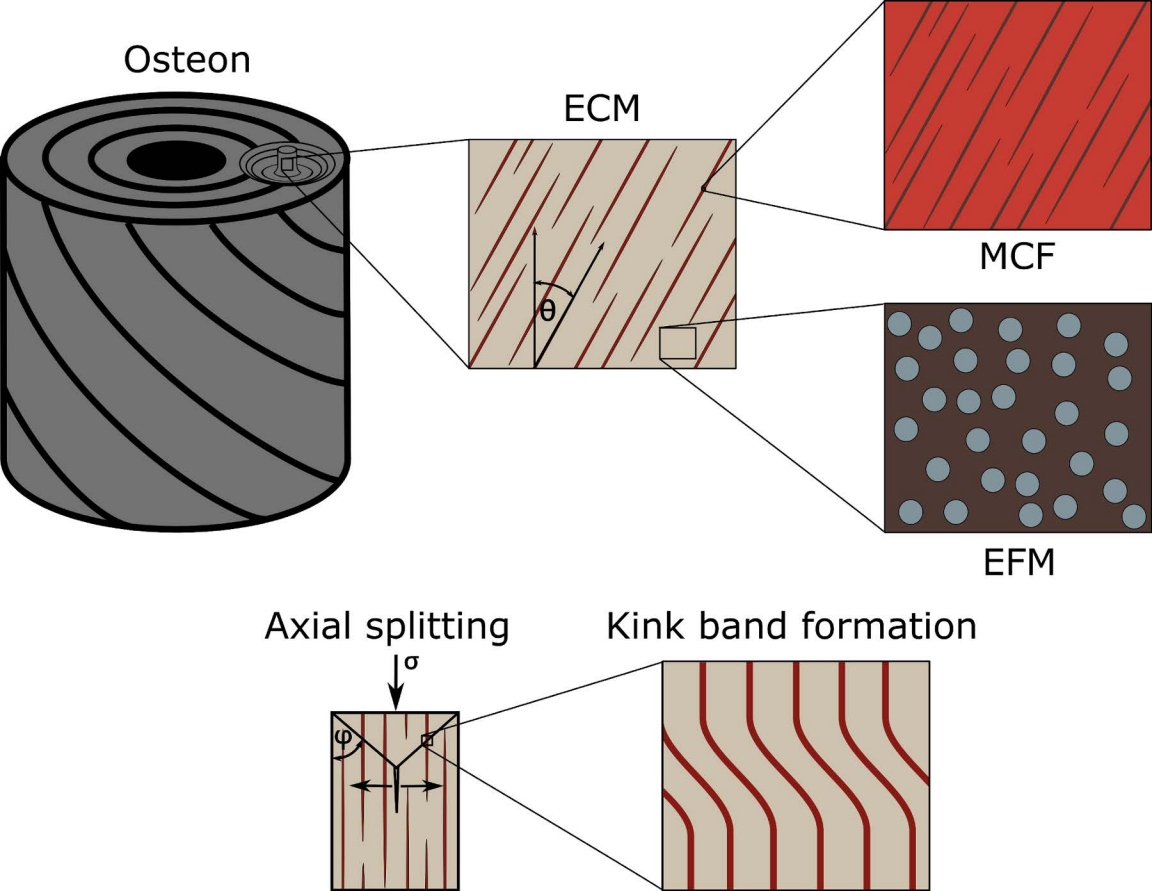
Osteon
ECM
θ
MCF
EFM
Axial splitting
σ
φ
Kink band formation

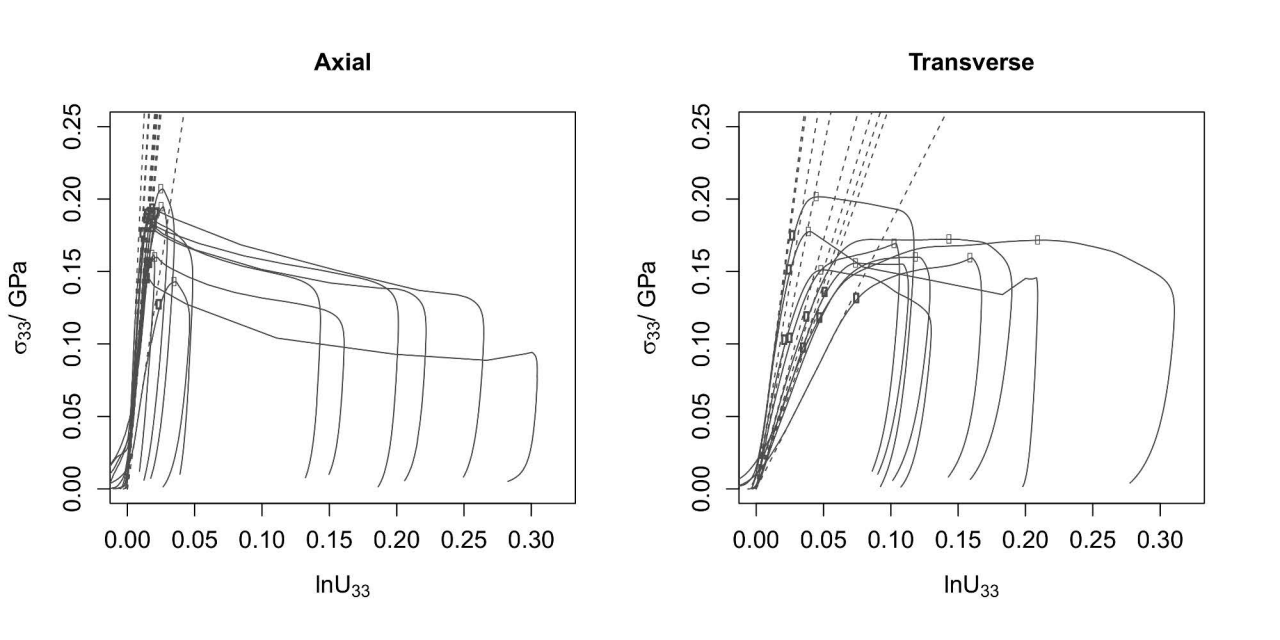
Axial
Transverse
σ33/ GPa
lnU33
0.00
0.05
0.10
0.15
0.20
0.25
0.30

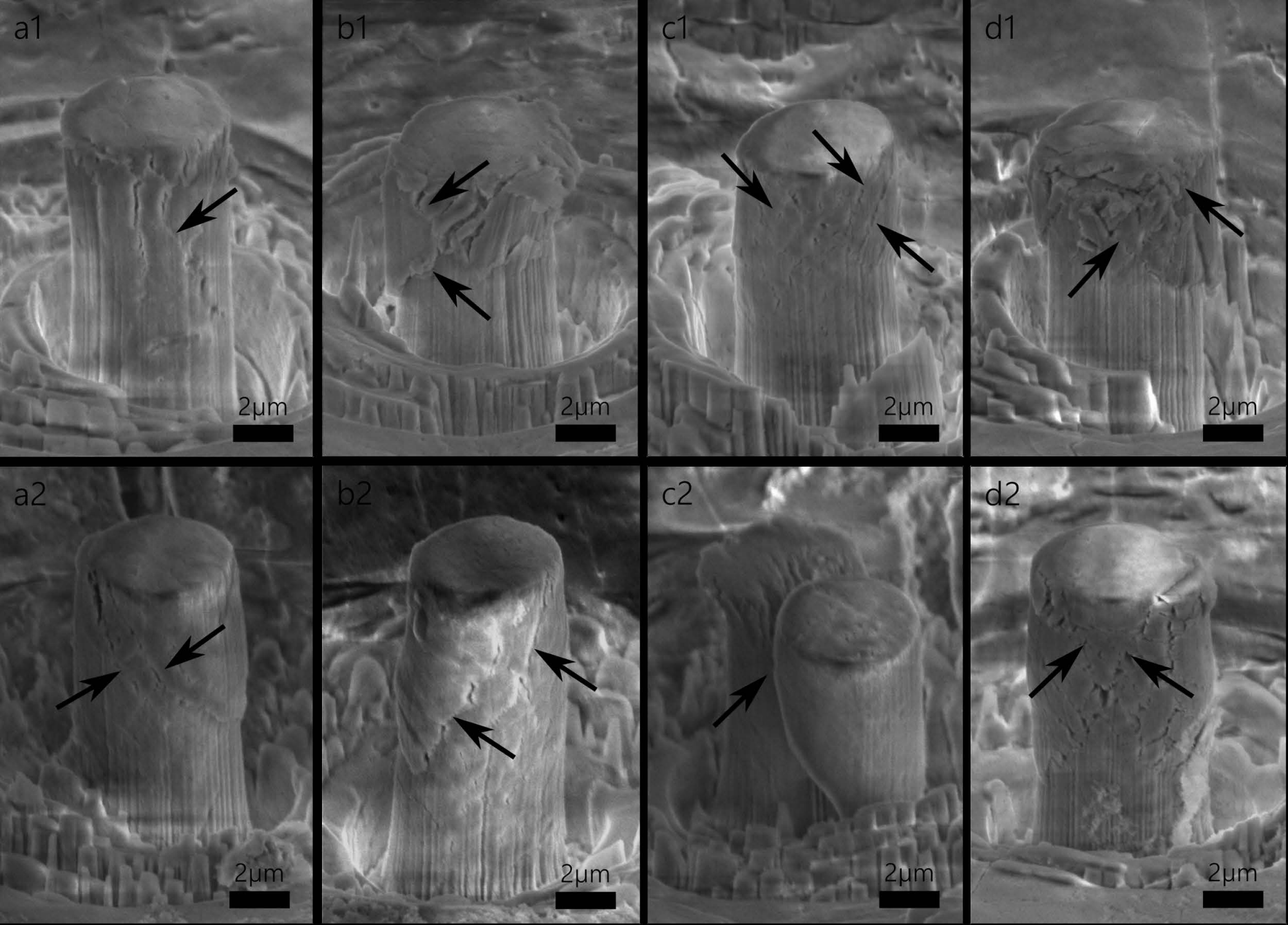
a1
b1
c1
d1
2μm
2μm
2μm
2μm
a2
b2
c2
d2
2μm
2μm
2μm
2μm

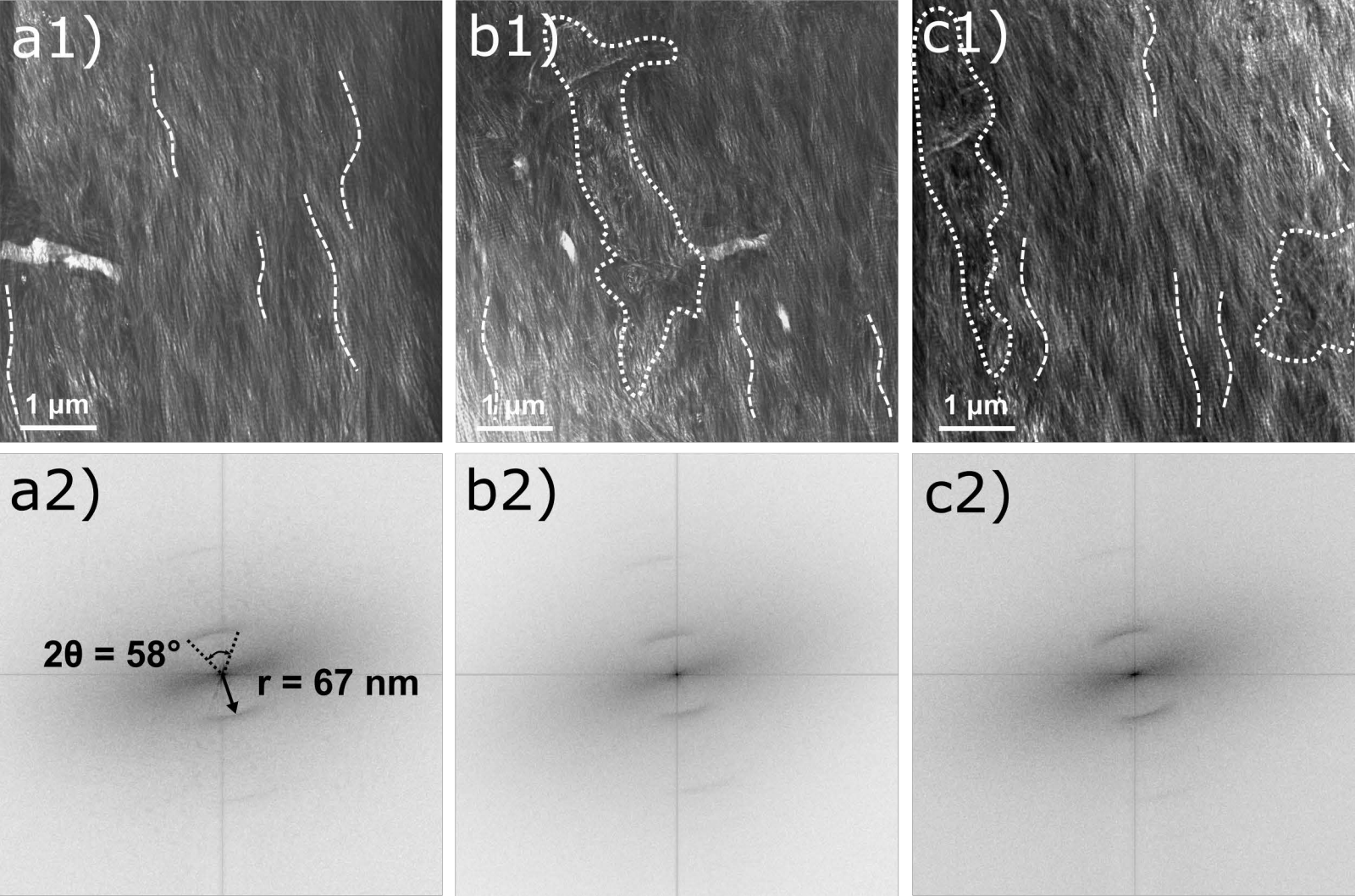
a1)
1 µm
b1)
1 µm
c1)
1 µm
a2)
2θ = 58°
r = 67 nm
b2)
c2)

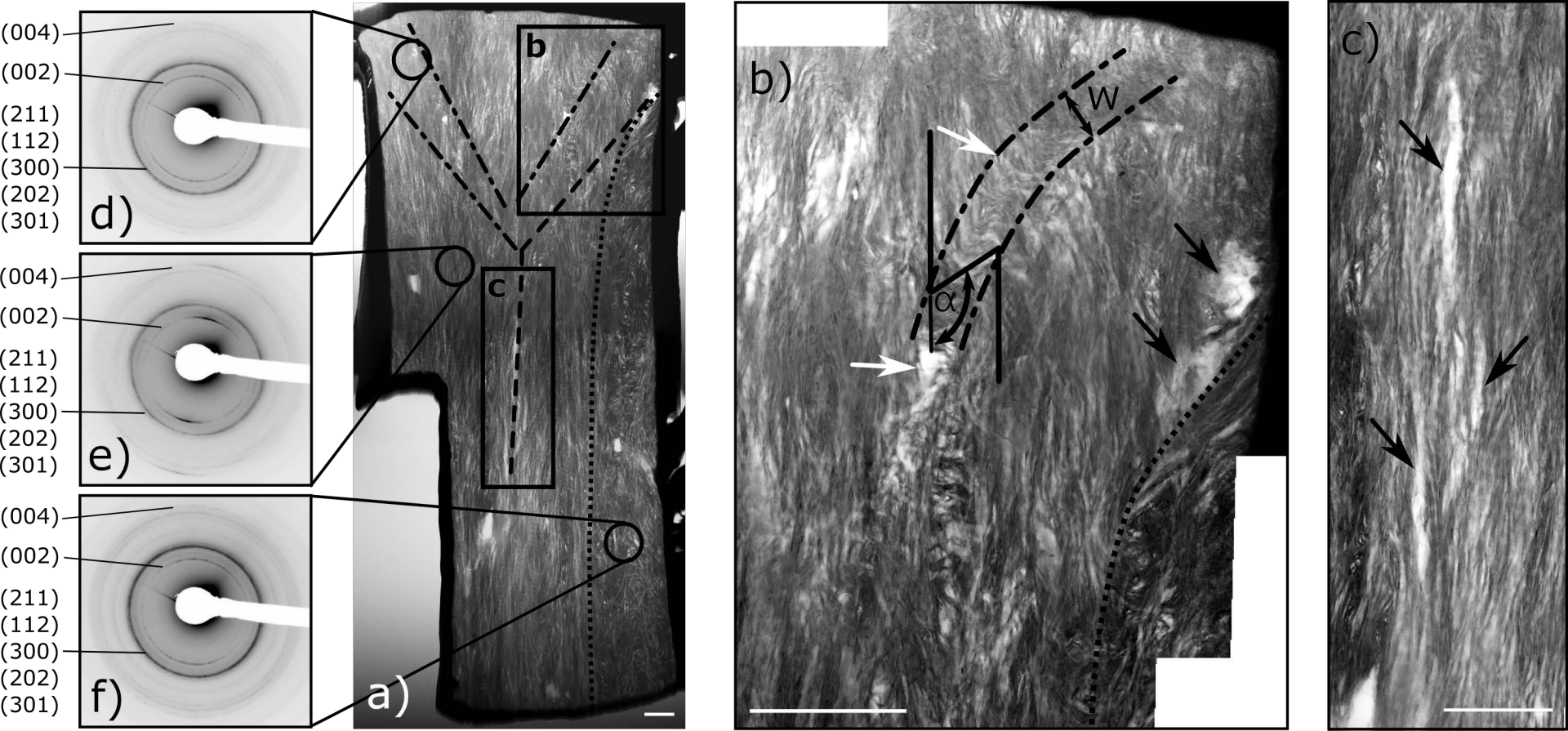
(004)
(002)
(211)
(112)
(300)
(202)
(301)
d)
e)
f)
a)
b
c
b)
W
α
c)

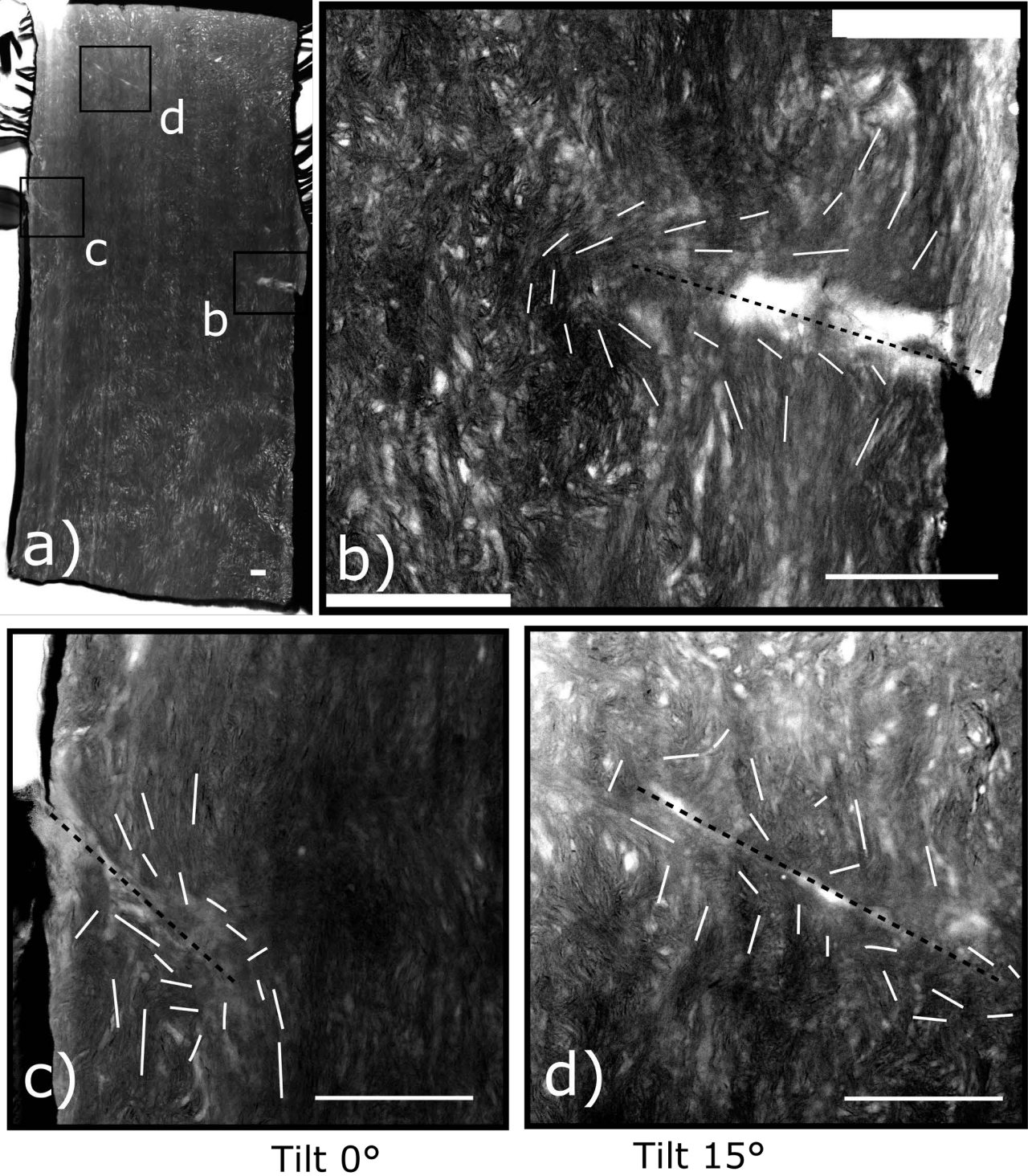

Tilt 0°

Tilt 15°